



A better understanding of hydroxyl radical photochemical sources in cloud waters collected at the puy de Dôme station – experimental versus modelled formation rates

A. Bianco^{1,2,*}, M. Passananti^{1,2,*}, H. Perroux^{3,4}, G. Voyard^{1,2}, C. Mouchel-Vallon^{3,4}, N. Chaumerliac^{3,4}, G. Mailhot^{1,2}, L. Deguillaume^{3,4}, and M. Brigante^{1,2}

¹Université Clermont Auvergne, Université Blaise Pascal, Institut de Chimie de Clermont-Ferrand, BP 10448, 63000 Clermont-Ferrand, France

²CNRS, UMR 6296, ICCF, 63171 Aubiere, France

³Université Clermont Auvergne, Université Blaise Pascal, Laboratoire de Météorologie Physique, BP 10448, 63000 Clermont-Ferrand, France

⁴CNRS, UMR 6016, LaMP, 63171 Aubiere, France

*These authors contributed equally to this work.

Correspondence to: L. Deguillaume (l.deguillaume@opgc.univ-bpclermont.fr)
and M. Brigante (marcello.brigante@univ-bpclermont.fr)

Received: 15 April 2015 – Published in Atmos. Chem. Phys. Discuss.: 18 May 2015

Revised: 15 July 2015 – Accepted: 30 July 2015 – Published: 19 August 2015

Abstract. The oxidative capacity of the cloud aqueous phase is investigated during three field campaigns from 2013 to 2014 at the top of the puy de Dôme station (PUY) in France. A total of 41 cloud samples are collected and the corresponding air masses are classified as highly marine, marine and continental. Hydroxyl radical ($\text{HO}\cdot$) formation rates ($R_{\text{HO}\cdot}^f$) are determined using a photochemical setup (xenon lamp that can reproduce the solar spectrum) and a chemical probe coupled with spectroscopic analysis that can trap all of the generated radicals for each sample. Using this method, the obtained values correspond to the total formation of $\text{HO}\cdot$ without its chemical sinks. These formation rates are correlated with the concentrations of the naturally occurring sources of $\text{HO}\cdot$, including hydrogen peroxide, nitrite, nitrate and iron. The total hydroxyl radical formation rates are measured as ranging from approximately 2×10^{-11} to $4 \times 10^{-10} \text{ M s}^{-1}$, and the hydroxyl radical quantum yield formation ($\Phi_{\text{HO}\cdot}$) is estimated between 10^{-4} and 10^{-2} . Experimental values are compared with modelled formation rates calculated by the model of multiphase cloud chemistry (M2C2), considering only the chemical sources of the hydroxyl radicals. The comparison between the experimental and the modelled results suggests that the photoreactivity of the iron species as a source of $\text{HO}\cdot$ is overestimated by the model, and H_2O_2

photolysis represents the most important source of this radical (between 70 and 99 %) for the cloud water sampled at the PUY station (primarily marine and continental).

1 Introduction

In the atmosphere, many trace gases are transformed by the hydroxyl radical ($\text{HO}\cdot$), which is considered the most efficient environmental oxidant (e.g. Seinfeld and Pandis, 2006). Evaluating the production of this short-lived species is crucial because it determines the fate of many chemical compounds. In atmospheric water drops and aqueous particles, the hydroxyl radical also controls the fate of inorganic and organic species (Herrmann et al., 2010). The $\text{HO}\cdot$ -mediated oxidation of organic compounds in the aqueous phase can lead to the formation of shorter but often multifunctional organic species and, ultimately, to complete mineralization (Charbouillot et al., 2012). Complex chemical reactions catalysed by $\text{HO}\cdot$ can also occur in the aqueous phase forming accretion products such as oligomers (Altieri et al., 2008; Carlton et al., 2007; Perri et al., 2009; Tan et al., 2012; Ervens and Volkamer, 2010; De Haan et al., 2009). These alternative

chemical pathways are efficient processes to convert organic compounds into secondary organic aerosols (SOAs) (Ervens et al., 2011).

The sources of hydroxyl radicals in the aqueous phase strongly differ from those in the gas phase because of the presence of ionic species and metal ions. Aqueous phase reactants that produce HO• present high concentrations in water drops and aqueous particles, likely enhancing the HO• photochemical production in the condensed phase. This radical can be generated in the aqueous phase by direct photolysis of hydrogen peroxide (H₂O₂) (Herrmann et al., 2010; Yu and Barker, 2003), iron complexes (Deguillaume et al., 2005), nitrate (NO₃⁻) (Zellner et al., 1990) and nitrite ions (NO₂⁻) (Zafriou and Bonneau, 1987). The other significant source of HO• in cloud water is the uptake from the gas phase (Arakaki and Faust, 1998). The relative importance of the different hydroxyl radical sources depends on the chemical composition of the aqueous phase, which is also strongly variable (Deguillaume et al., 2014). HO• is further scavenged in the aqueous phase, primarily by dissolved organic compounds. Evaluation of this sink is difficult because the dissolved organic matter is diverse, complex and poorly characterized (Herckes et al., 2013).

Uncertainties in HO• sinks and sources make its concentrations in atmospheric water highly difficult to estimate. For this estimation, models describing the multiphase cloud chemistry have been developed and have considered the reactivity in the gas and aqueous phases along with the mass transfer between the two phases (Ervens et al., 2014; Long et al., 2013; Tilgner and Herrmann, 2010). These numerical tools allow for the estimation of the steady-state concentration of HO• ([HO•]_{ss}), which is a crucial quantity to understand the fate of atmospheric pollutants (Arakaki et al., 2013). The range of the maximal HO• concentration varies from 10⁻¹⁶ to 10⁻¹² M, depending on the “chemical scenario” (i.e. emission/deposition and the initial chemical conditions) used in the modelling study. The amounts of organic matter and iron are key parameters controlling the [HO•]_{ss}. These models are expected to underestimate the radical sinks because organic scavengers cannot be exhaustively described in the aqueous chemical mechanism (Arakaki et al., 2013).

In this study, we propose the investigation of the hydroxyl radical formation in real cloud water sampled at the puy de Dôme (PUY; France). The hydroxyl radical formation rate is quantified for 36 cloud water samples collected during three field campaigns (2013–2014). Because the main photochemical sources (hydrogen peroxide, iron, nitrite and nitrate) are also quantified, we can calculate their relative contributions to the production of the hydroxyl radicals. For this purpose, the contribution to the hydroxyl radical formation rate of more concentrated inorganic photochemical sources is investigated separately in a synthetic solution. In parallel, the model of multiphase cloud chemistry (M2C2) is used to simulate HO• formation rates. This model considers explicit

aqueous chemical mechanisms, and a “simplified” version of the model is used to reproduce the bulk water irradiation experiments (lamp spectrum) under variable physico-chemical conditions (pH, initial concentrations of HO• sources) corresponding to the cloud water samples. The comparison between the modelled and experimental HO• production rates facilitates quantification of the various HO• sources and enables validation of the model to reproduce the oxidative capacity of the atmospheric aqueous phase.

2 Materials and methods

2.1 Chemicals

Hydrogen peroxide (30% in water, not stabilized), sodium nitrate (purity > 99%) and ferrozine (purity > 97%) were obtained from FLUKA, while sodium nitrite (purity > 98%) and terephthalic disodium salt (purity > 99%) were purchased from Prolabo and Alfa Aesar, respectively. All of the other chemicals (purity reagent grade) used for the analysis were obtained from Sigma-Aldrich.

Solutions are prepared with deionized ultra-pure aerated Milli-Q water from Millipore (resistivity = 18.2 MΩ cm) under a laminar flux hood. Moreover, glass containers and injection material are washed 3 times with ultrapure water before use. If necessary, the pH values are adjusted with perchloric acid (1 N) and NaOH (1 N) using a Jenway 3310 pH meter within ±0.01 pH units. All of the solutions are stored under dark conditions and the final preparations are performed in a room equipped with a sodium lamp (589 nm emission).

2.2 Cloud water sampling

Cloud water is sampled at the PUY station (48° N, 2° E; 1465 m a.s.l.) in the Massif Central region (France). Three campaigns occurred during autumn 2013 from 14 October to 6 November, during spring and autumn 2014 from 22 March to 5 April and from 4 to 19 November. During these periods, the station was primarily located in the free troposphere; thus, the air masses from various origins were not influenced by the local pollution (Hervo, 2013).

The cloud droplet sampling is performed by a one-stage cloud droplet impactor (Deguillaume et al., 2014). With the air flux used, the lower limit of the aerodynamic diameter is approximately 7 μm (Brantner et al., 1994). The impactor used for this study is constructed of stainless steel and aluminum, and cloud droplets are collected by impaction onto a rectangular aluminum plate with an average sampling time of 2 h. Cloud water samples are filtered using a 0.45 μm PTFE (polytetrafluoroethylene) filter within 10 min after sampling to eliminate all of the microorganisms and particles that can interfere with the spectroscopic analysis.

Measurements performed immediately after cloud collection are conductivity, redox potential, pH, UV-visible spec-

troscopy, H₂O₂ and iron concentrations. Ion chromatography (IC), total organic carbon (TOC), and nitrite analysis are determined less than 24 h after sampling. At each stage, sampling and analyses are performed with the greatest precaution to minimize all possible external contaminations and the solutions are stored at 277 K under dark conditions. Hydroxyl radical formation rates ($R_{\text{HO}\cdot}^{\text{f}}$) and polychromatic quantum yields ($\Phi_{\text{HO}\cdot}$) are calculated using polychromatic wavelengths.

2.3 Physico-chemical measurements

Different parameters are monitored, including pH, conductivity and redox potential, which are measured using a Hanna multiparameter instrument. The UV–visible spectrum of the collected cloud water is determined with an Agilent Technologies Cary 60 UV–visible spectrophotometer. The TOC concentration is determined with a TOC 5050A analyser (Shimadzu). Hydrogen peroxide concentration is estimated using *p*-hydroxyphenylacetic acid (HPAA, purity > 98 %) and horseradish peroxidase (POD) (solid containing 150–200 units per milligram), according to the spectrofluorimetric quantification method (Miller and Kester, 2002). The formation of the dimer of HPAA is correlated with the concentration of hydrogen peroxide and is detected using a Varian Cary Eclipse fluorescence spectrophotometer setting excitation wavelengths at 320 nm, while emission is registered from 340 and 500 nm. The maximum signal is quantified at 408 nm. The scan rate is 600 nm min⁻¹, and a bandpass of 10 nm is set for excitation and emission. The nitrite ions concentration is determined by derivatization with 2,4-dinitrophenylhydrazine (DNPH) (purity > 97 %), in acidic solution (HCl 37 %). The UV-absorbing derivative (2,4-dinitrophenylazide) is detected by HPLC. The HPLC system (Waters Alliance) equipped with a diode array detector is used with an Eclipse XDB-C18 column (Agilent, 4.6 × 150 mm, 5 μm) and an isocratic method is adopted using 40 % acidified water (0.1 % phosphoric acid) and 60 % methanol. The flow rate is 1 mL min⁻¹, and 2,4-dinitrophenylazide is eluted with a retention time of 4.1 min (Kieber and Seaton, 1995) and detected at 307 nm. Fe(II) and Fe(III) concentrations are determined by the spectrophotometric method by complexation with ferrozine (purity > 97 %), as described by Stookey (1970). Fe(II) and Fe(III) represent the oxidative state of the iron species. The adopted complexation method allows us to determine all Fe(II) and Fe(III) species present in solution (i.e. considered as free, aqua complexes and as complex with other organic molecules). Ascorbic acid (purity reagent grade) is used as the reducing agent to determine total iron. The complex absorption is measured with a Varian Cary 300 scan spectrophotometer at 562 nm.

It has been previously demonstrated that filtration does not modify the soluble iron quantification in natural cloud water samples (Parazols et al., 2006; Vaitilingom et al., 2013). It

is not possible to measure particulate iron because the ferrozine method cannot solubilize solid phase-iron (the contact time between acidic reagents and particulate iron is too short). Moreover, the iron particle is expected to be less reactive than the solubilized iron; consequently, its contribution can be neglected (Arakaki and Faust, 1998).

Ion chromatography (IC) analysis is performed employing a Dionex DX-320 equipped with an IonPac AG11 (guard-column 4 × 50 mm) and an IonPac AS11 (analytical column 5 × 250 mm) for anions and a Dionex ICS-1500 equipped with an IonPac CG16 (guard-column 4 × 50 mm) and an IonPac CS16 (analytical column 5 × 250 mm) for cations.

2.4 Statistical analysis

The principal component analysis (PCA) and hierarchical clustering analysis (HCA) are performed with R 3.1.2 software (R Core Team, 2013) using the FactoMineR package (version 1.28; Lê et al., 2008). This statistical analysis provides a synthetic representation of experimental data as a function of the correlations between variables considered and similarities present among the analysed samples. This technique allows for the determination of information contained in a set of multivariate data, summarizing it in a few linear combinations of the variables (Deming et al., 1988). HCA data are grouped by similarity, considering all of the information contained in the data set. HCA is a statistical method to qualitatively study the composition of cloud water and can be used to identify the grouping variables that are not well detectable using only PCA.

2.5 Irradiation experiments

To evaluate the contribution of each possible photochemical source (nitrate, nitrite or hydrogen peroxide) to the hydroxyl radical formation in cloud water, synthetic solutions doped with a single source of oxidant are irradiated to quantify their contribution to the total generation of hydroxyl radicals in a more complex medium.

The photochemical device is composed of a xenon lamp equipped with a water cooler to avoid the increase of temperature due to the infrared radiations and a mirror to reflect the light vertically. A Pyrex filter was located before the reactor to filter light at wavelengths below 290 nm, corresponding to the lowest wavelengths of the solar emission spectrum. The reactor is a 40 mL cylindrical Pyrex container cooled by water circulation at a temperature of 278 ± 2 K to limit thermal reactions. Samples are continuously stirred with a magnetic stirrer using a Teflon bar to ensure homogeneity.

In Fig. 1, the emission spectrum of the lamp recorded using fiber optics coupled with a charge-coupled device (CCD) spectrophotometer (Ocean Optics USD 2000+UV-VIS) is reported. The energy was normalized with the actinometry results using a paranitroanisole (PNA)/pyridine actinometer (Dulin and Mill, 1982). Over the wavelength range of 290–

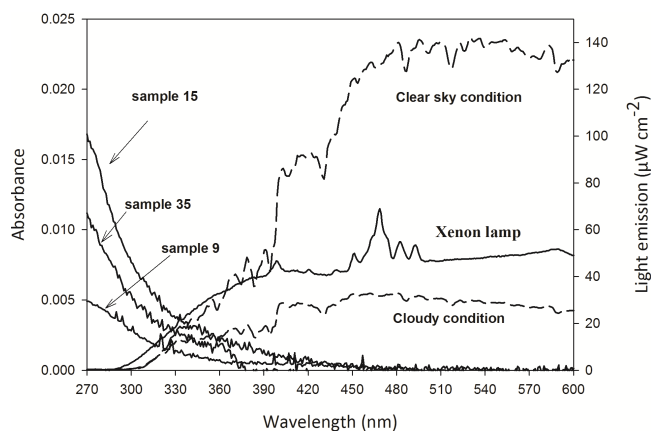


Figure 1. Absorption spectra of different cloud water samples on the left axis; the right axis shows the emission spectrum of the adopted xenon lamp reaching solutions over the range of 290–600 nm (total flux intensity = 157 W m^{-2}) compared with the sun emission spectrum (dashed line) for a sunny (353 W m^{-2}) and a cloudy day (90 W m^{-2}) in October 2013.

600 nm, a total flux of 157 W m^{-2} is measured. The intensity values of the sun's emissions under clear-sky and cloudy conditions at puy de Dôme in autumn 2013 are also presented in Fig. 1.

2.6 Hydroxyl radical formation rate and quantum yield determination

The hydroxyl radical formation rate is determined using terephthalate (TA) (terephthalic disodium salt, purity > 99 %) as a probe (Charbouillot et al., 2011). Formation of hydroxyterephthalate (TAOH) is quantified using a Varian Cary Eclipse fluorescence spectrophotometer, setting excitation wavelengths at 320 nm while the emission maximum is measured at 420 nm. The scan rate is 600 nm min^{-1} and a bandpass of 10 nm is set for excitation and emission. Terephthalate is a useful probe because it allows for the determination of hydroxyl radical formation rates in the presence of fluorescent dissolved organic matter. The concentration of the probe is in a large excess (2 mM) compared with the concentration of organic matter to trap all of the photo-generated hydroxyl radicals and then to estimate a value for the hydroxyl radical formation rate not affected by depletion of $\text{HO}\cdot$ by other sinks.

The reaction between TA and the hydroxyl radical leads to the formation of fluorescent TAOH and non-fluorescent secondary products (Reaction R1) as follows:



The degradation rate of TA (R_{TA}^{d}) and formation rates of the hydroxyl radical ($R_{\text{HO}\cdot}^{\text{f}}$) and TAOH ($R_{\text{TAOH}}^{\text{f}}$) can be ex-

pressed as follows:

$$R_{\text{HO}\cdot}^{\text{f}} \approx R_{\text{TA}}^{\text{d}} \approx \frac{R_{\text{TAOH}}^{\text{f}}}{\gamma}, \quad (1)$$

with

$$R_{\text{TA}}^{\text{d}} = k_{\text{HO}\cdot, \text{TA}} [\text{HO}\cdot] [\text{TA}], \quad (2)$$

where $k_{\text{HO}\cdot, \text{TA}} = 4.0 \times 10^9 \text{ M}^{-1} \text{ s}^{-1}$ is the second-order rate constant of the reaction between $\text{HO}\cdot$ and TA (Charbouillot et al., 2011), [TA] is the initial concentration of terephthalate and γ is the TAOH formation yield calculated as a function of solution pH. This value is found to be linearly correlated with the pH value and is estimated between the values of 0.15 and 0.25 over the pH range of 4–7.

Other radicals, such as sulfate ($\text{SO}_4^{\cdot-}$) or chlorine/dichlorine ($\text{Cl}\cdot/\text{Cl}_2^{\cdot-}$), can react with TA, leading to the H abstraction as first chemical reaction. However, their direct generation is nearly exclusively due to the electron transfer reaction from the corresponding anion (i.e. SO_4^{2-} and Cl^- , respectively) to the hydroxyl radical. Moreover, considering that the second-order rate constant of aromatic compounds with the dichloride radical anion and the sulfate radical is expected to be 1 or 2 orders of magnitude lower than that with the hydroxyl radical (Neta et al., 1988), and considering a relatively low concentration of sulfate and dichlorine radicals in our cloud samples, the TA reactivity can be attributed exclusively to the $\text{HO}\cdot$.

The quantum yield of hydroxyl radical formation ($\Phi_{290-400 \text{ nm}}^{\text{HO}\cdot}$) is defined as the ratio between the formation rate of $\text{HO}\cdot$ ($R_{\text{HO}\cdot}^{\text{f}}$) and the number of absorbed photons in einstein per unit of time in the overlap range of 290–600 (λ_1 and λ_2) (Eq. 3).

This value evaluates the photochemical process efficiency independently of the experimental photochemical conditions.

$$\Phi_{290-400 \text{ nm}}^{\text{HO}\cdot} = \frac{R_{\text{HO}\cdot}^{\text{f}}}{I_a}, \quad (3)$$

where I_a can be calculated from the following equation:

$$I_a = \int_{\lambda_1}^{\lambda_2} I_0(\lambda) (1 - 10^{-\text{Abs}(\lambda)}) d\lambda, \quad (4)$$

where I_0 (photons $\text{m}^{-2} \text{ s}^{-1}$) is the incident photon flux corresponding to the lamp emission and Abs is the absorption of cloud water (normalized considering the optical path length of 5 cm inside of the thermostated reactor).

2.7 Back-trajectory plots

Backward trajectories of collected air masses are calculated using the HYSPLIT (HYbrid Single-Particle Lagrangian Integrated Trajectory) model with the GDAS1 (Global

Data Assimilation System) meteorological data archive and the model of vertical velocity (<http://ready.arl.noaa.gov/HYSPLIT.php>, HYSPLIT, 2012). Backward trajectories are calculated for 72 h.

2.8 Model description

The M2C2 combines detailed multiphase chemistry along with the parameterization of the microphysics (Leriche et al., 2001, 2000; Deguillaume et al., 2004). In particular, the detailed chemistry of H_xO_y , chlorine, carbonates, NO_y , sulfur, transition metal ions (iron, copper, manganese) and the oxidation of volatile organic compounds (VOCs) is included. Photolysis rates are calculated in the gaseous and aqueous phases, and the pH is calculated following the H^+ concentration. Numerical results consist of following the time evolution of the concentrations of each chemical species and calculating at each time step the relative contribution of chemical reactions in the production/destruction of chemical compounds.

In this study, a simplified version of the model is used. The cloud chemical mechanism is restricted to inorganic chemistry (H_xO_y , nitrogen, iron) that leads to the $HO\cdot$ formation (see Table S1 in the Supplement for details about the considered reactions). The complexation of iron by oxalate is also considered in the model because it can interfere with the $HO\cdot$ formation rates (Long et al., 2013). Laboratory irradiation experiments are simulated with the M2C2 model considering its chemical module and neglecting microphysical processes and mass transfer parameterizations. Temperature and pH remained constant during the simulation time. We set the pH for each cloud water sample to the values reported in Table S2 and the temperature is fixed at 278 K, which corresponds to the temperature of the irradiated solutions. The simulated irradiation intensity is held constant and homogenous throughout the experiment. The actinic flux of the experimental lamp is discretized in the tropospheric ultraviolet–visible (TUV) model in 156 non-regular intervals over a wavelength range of 120–750 nm (Madronich and Flocke, 1999). The photolysis rates of the chemical species are calculated in TUV according to the experimental quantum yields and absorption cross sections and are indicated in Table S1. Experimental chemical concentrations (Table S2) are used to initialize the model (H_2O_2 , nitrite, nitrate, iron). Moreover, oxalic acid is considered as an organic complexant during the Fe(II)/Fe(III) cycle. The formation rate of $HO\cdot$ is calculated by the model considering the modelled contribution of each reaction producing $HO\cdot$ during 1 h of experiment.

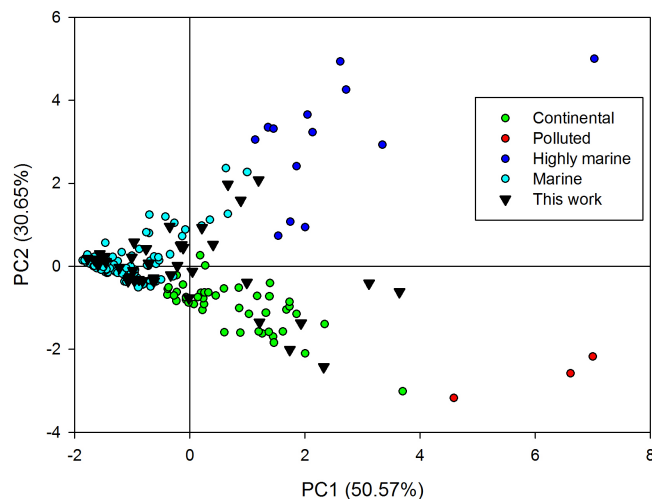


Figure 2. Scores plot obtained by PCA analysis of 137 samples (corresponding to 73 cloud events) collected before 2013 and grouped in four classes in function of the previously described classification (Deguillaume et al., 2014) and 41 samples (numbered from 80 to 120) collected during 2013 and 2014. These new data correspond to 15 cloud events and are indicated in black triangles. Statistical analysis is performed using six selected variables (pH, $[Na^+]$, $[Cl^-]$, $[SO_4^{2-}]$, $[NO_3^-]$, and $[NH_4^+]$). The scree plot obtained from autoscaled data shows two selected principal components (PCs) containing a total variance of about 81 %.

3 Results and discussion

3.1 Classification of cloud samples

Recently, physicochemical parameters and concentrations of the major organic and inorganic compounds of cloud samples collected over the last 10 years at the puy de Dôme are measured and statistically analysed by PCA (Deguillaume et al., 2014). Along with the corresponding back-trajectory plots, four different categories of air masses reaching the summit of the PUY could be distinguished as polluted, continental, marine and highly marine. Highly marine clouds exhibited high concentrations of Na^+ and Cl^- , and the marine category presented a lower concentration of ions but more elevated pH, while the two remaining clusters, classified as continental and polluted, are characterized by the second-highest and highest levels of NH_4^+ , NO_3^- , and SO_4^{2-} , respectively.

In Table S2, the measured physico-chemical composition of the cloud water samples is reported for this study. We use the same statistical analysis to classify these cloud water samples as Deguillaume et al. (2014). PCA is performed using the pH and the concentration of sulfate, nitrate, chloride, sodium and ammonium ions as variables. Figure 2 reports the scores plot for samples used for the previously reported classification as a function of the attributed class and for the new samples. Three types are identified as (i) highly marine, (two samples) characterized by pH values of 5.0 and 5.6, respec-

Table 1. Concentration of main sources of hydroxyl radical in sampled clouds. A total of 41 samples have been analysed. BDL: below detection limit (0.01 μM for iron and 0.05 μM for NO_2^-). NM: not measured.

Sample	iron (μM)		H_2O_2 (μM)	NO_3^- (μM)	NO_2^- (μM)	Sample	iron (μM)		H_2O_2 (μM)	NO_3^- (μM)	NO_2^- (μM)
	II	III					II	III			
1	NM	NM	12.3	16.7	0.46	22	BDL	BDL	52.3	131.9	0.72
2	NM	NM	9.0	6.1	1.44	23	BDL	BDL	49.4	133.1	0.95
3	NM	NM	15.1	9.9	0.40	24	BDL	BDL	8.1	7.5	BDL
4	NM	NM	14.0	14.2	0.30	25	0.08	0.02	6.7	21.2	0.15
5	NM	NM	13.0	14.7	0.38	26	0.40	0.20	6.8	39.7	BDL
6	NM	NM	7.8	2.6	BDL	27	0.70	0.20	6.6	75.6	BDL
7	NM	NM	6.2	1.7	BDL	28	0.70	0.30	7.2	73.8	BDL
8	NM	NM	9.7	6.9	BDL	29	0.01	0.10	8.0	24.7	0.27
9	NM	NM	8.2	8.2	BDL	30	BDL	0.16	8.8	19.7	0.52
10	NM	NM	10.2	2.3	BDL	31	BDL	0.45	9.1	20.7	0.61
11	NM	NM	17.2	5.6	BDL	32	BDL	BDL	13.1	21.4	0.07
12	BDL	0.57	18.0	24.7	0.28	33	BDL	0.10	2.1	6.1	BDL
13	BDL	0.12	24.6	23.7	1.10	34	0.09	BDL	8.4	10.3	0.47
14	BDL	0.11	12.0	19.0	BDL	35	BDL	BDL	2.2	15.1	0.51
15	BDL	BDL	14.5	19.0	0.23	36	BDL	0.03	2.1	20.3	BDL
16	BDL	BDL	9.1	21.3	0.10	37	BDL	0.03	2.1	18.5	BDL
17	BDL	0.11	16.2	219.6	0.05	38	0.07	BDL	2.4	13.5	0.34
18	0.10	0.01	16.2	205.6	0.07	39	0.04	BDL	3.1	20.8	BDL
19	BDL	BDL	14.9	20.0	0.12	40	BDL	0.01	5.7	39.1	BDL
20	BDL	BDL	15.7	37.4	0.19	41	BDL	0.02	5.3	46.5	0.16
21	BDL	BDL	22.2	72.6	0.42						

tively, high concentration of chloride and sodium and low concentrations of nitrate, nitrite and ammonium; (ii) marine cloud waters (28 samples), showing pH values between 4.7 and 7.6 and very low concentrations of anions and cations; and (iii) continental samples (11 samples), with pH values from 4.1 to 6.9 and a medium concentration of nitrates, sulfates and ammonium, while sodium and chloride concentrations are very low. No sample could be classified as polluted cloud water because polluted cloud waters have been characterized by concentrations of nitrates, sulfates and ammonium higher than 350, 70 and 330 μM , respectively. This statistical analysis confirms that the majority of the collected samples are of marine origin. This statistical analysis is confirmed by the back-trajectory plots from the HYSPLIT model, showing that most of the air masses reaching the puy de Dôme arise from the west sector i.e. from the Atlantic Ocean.

3.2 Determination of the hydroxyl radical formation rates and photolysis rates

The concentration of the main photochemical sources of $\text{HO}\cdot$ for each sample is reported in Table 1. In particular, the Fe(II) and Fe(III) concentrations are below the detection limit (0.01 μM) for the majority of the collected samples. The highest value found for the Fe(II) concentration is 0.7 μM , while it is 0.6 μM for Fe(III), corresponding to typical values found for marine origin cloud waters (Parazols et al., 2006).

The H_2O_2 concentration values range between 6 and 50 μM and nitrate is evaluated between 2 and 220 μM , while the nitrite concentration is between 0 and 1.4 μM .

The $R_{\text{HO}\cdot}^f$ was measured in pure water doped with different concentrations of hydrogen peroxide, nitrate and nitrite on the same order of magnitude as the collected natural samples. The conditions were those used for natural cloud samples (see Sect. 2.6). A linear correlation between $R_{\text{HO}\cdot}^f$ and the concentrations of photochemical precursors is found (Fig. 3). The photolysis rate (J) (s^{-1}) is then estimated from the slopes and reported in Table 4. For H_2O_2 , the J value is half of the experimental slope because H_2O_2 provides two $\text{HO}\cdot$ radicals.

$R_{\text{HO}\cdot}^f$ is determined for 36 samples, and its value is estimated between 3.3×10^{-12} and $4.2 \times 10^{-10} \text{M s}^{-1}$. Higher values are obtained for cloud water samples of continental origin, while the values found for marine and highly marine cloud waters are less than $1.4 \times 10^{-10} \text{M s}^{-1}$. The quantum yield of the formation of hydroxyl radicals under polychromatic irradiation between 290 and 400 nm ($\Phi_{290-400\text{nm}}^{\text{HO}\cdot}$; see Eq. 3) is estimated as between 10^{-5} and 10^{-2} . (Table 2).

To our knowledge, only a scarce number of data are available in the literature concerning measurements of $R_{\text{HO}\cdot}^f$ and formation quantum yield ($\Phi^{\text{HO}\cdot}$) in real cloud waters (Table 3). Faust and Allen (1993) measured the photoformation rates of $\text{HO}\cdot$ (ranging from 1.3 to $8.3 \times 10^{-10} \text{M s}^{-1}$) under

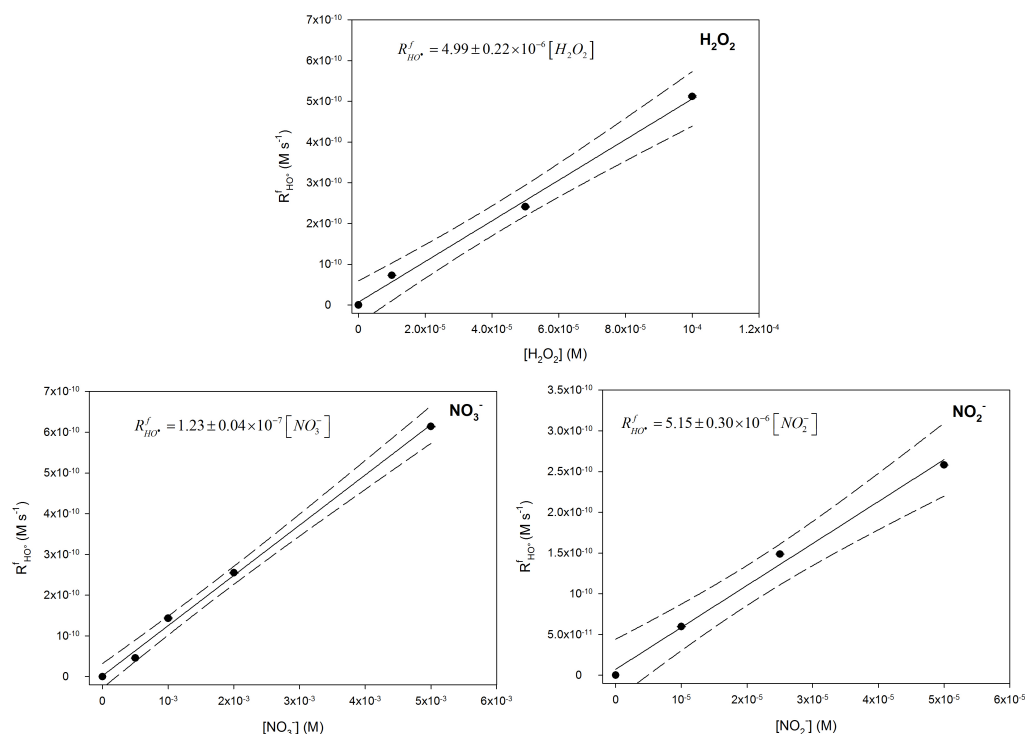


Figure 3. Scatter plots of hydroxyl radical formation rates vs. hydrogen peroxide, nitrate and nitrite concentrations using 2 mm of TA at pH 5.0 under xenon lamp irradiation. The solid line is the linear fit and dashed lines denote the 90 % confidence of the linear fit.

Table 2. $R_{\text{HO}\cdot}^f$ (M s^{-1}) and hydroxyl radical polychromatic quantum yield formation ($\Phi_{\text{HO}\cdot}^{290-400\text{nm}}$) values estimated from cloud water samples. NM: not measured. Mar: Marine. H-Mar: Highly Marine. Cont: Continental influence. The errors on $R_{\text{HO}\cdot}^f$ are derived at the 1σ level simply from the scattering of experimental data.

Sample	$R_{\text{HO}\cdot}^f$ (M s^{-1})	$\Phi_{\text{HO}\cdot}^{290-400\text{nm}}$	Class	Sample	$R_{\text{HO}\cdot}^f$ (M s^{-1})	$\Phi_{\text{HO}\cdot}^{290-400\text{nm}}$	Class
1	$(3.30 \pm 0.23) \times 10^{-11}$	1.27×10^{-3}	Mar	22	$(3.37 \pm 0.01) \times 10^{-10}$	2.5×10^{-3}	Cont
2	NM	NM	Mar	23	$(4.16 \pm 0.01) \times 10^{-10}$	1.8×10^{-3}	Cont
3	NM	NM	Mar	24	$(5.10 \pm 0.01) \times 10^{-10}$	NM	Mar
4	$(1.40 \pm 0.01) \times 10^{-10}$	1.0×10^{-2}	H-Mar	25	$(2.42 \pm 0.08) \times 10^{-11}$	1.9×10^{-4}	Cont
5	$(1.24 \pm 0.02) \times 10^{-10}$	6.0×10^{-3}	H-Mar	26	$(1.41 \pm 0.01) \times 10^{-10}$	3.4×10^{-3}	Cont
6	$(2.77 \pm 0.01) \times 10^{-11}$	1.5×10^{-4}	Mar	27	$(4.95 \pm 0.01) \times 10^{-11}$	1.5×10^{-4}	Cont
7	$(5.60 \pm 0.06) \times 10^{-11}$	9.0×10^{-3}	Mar	28	NM	NM	Cont
8	$(2.48 \pm 0.01) \times 10^{-11}$	2.9×10^{-3}	Mar	29	$(8.48 \pm 0.04) \times 10^{-11}$	1.3×10^{-4}	Mar
9	$(2.20 \pm 0.02) \times 10^{-11}$	1.8×10^{-3}	Mar	30	$(8.43 \pm 0.02) \times 10^{-11}$	1.2×10^{-4}	Mar
10	$(2.93 \pm 0.02) \times 10^{-11}$	2.4×10^{-3}	Mar	31	$(6.11 \pm 0.21) \times 10^{-11}$	5.1×10^{-5}	Mar
11	$(6.77 \pm 0.02) \times 10^{-11}$	2.7×10^{-3}	Mar	32	NM	NM	Mar
12	$(6.10 \pm 0.19) \times 10^{-11}$	1.7×10^{-4}	Mar	33	$(3.27 \pm 0.23) \times 10^{-12}$	1.3×10^{-5}	Mar
13	$(4.66 \pm 0.01) \times 10^{-11}$	1.5×10^{-4}	Mar	34	$(2.73 \pm 0.01) \times 10^{-11}$	8.5×10^{-4}	Mar
14	$(2.81 \pm 0.01) \times 10^{-11}$	2.0×10^{-4}	Mar	35	$(3.60 \pm 0.30) \times 10^{-11}$	6.0×10^{-4}	Mar
15	$(1.09 \pm 0.04) \times 10^{-11}$	9.0×10^{-5}	Mar	36	$(5.97 \pm 0.12) \times 10^{-11}$	9.6×10^{-5}	Mar
16	NM	NM	Mar	37	$(2.41 \pm 0.04) \times 10^{-11}$	8.4×10^{-5}	Mar
17	$(6.05 \pm 0.44) \times 10^{-11}$	4.1×10^{-5}	Cont	38	$(5.76 \pm 0.13) \times 10^{-11}$	2.7×10^{-4}	Mar
18	$(3.39 \pm 0.20) \times 10^{-11}$	3.2×10^{-5}	Cont	39	$(2.69 \pm 0.04) \times 10^{-11}$	1.1×10^{-4}	Mar
19	$(8.11 \pm 0.02) \times 10^{-11}$	1.9×10^{-4}	Mar	40	$(1.27 \pm 0.01) \times 10^{-10}$	2.6×10^{-4}	Cont
20	$(8.46 \pm 0.01) \times 10^{-11}$	8.4×10^{-3}	Mar	41	$(1.09 \pm 0.01) \times 10^{-10}$	5.1×10^{-4}	Cont
21	$(1.54 \pm 0.01) \times 10^{-10}$	1.5×10^{-3}	Cont				

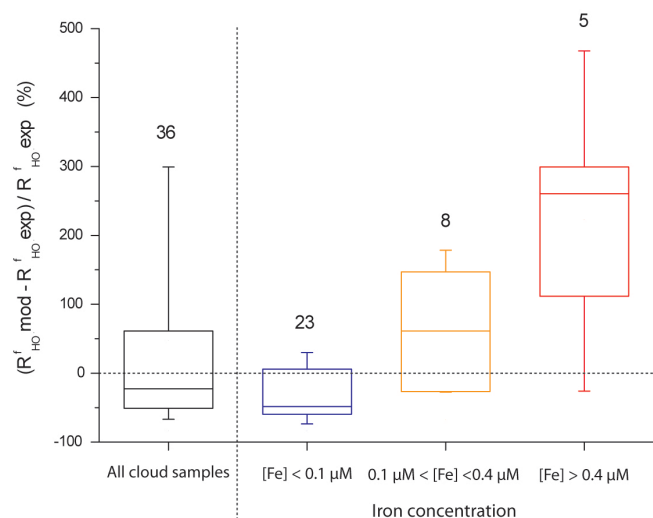


Figure 4. Distribution of the bias error for all cloud water samples (black) and for cloud samples discretized as a function of different iron concentration ranges (in colour). The bias error is defined by the ratio $(R_{\text{HO}\cdot}^{\text{f, mod}} - R_{\text{HO}\cdot}^{\text{f, exp}}) / R_{\text{HO}\cdot}^{\text{f, exp}}$ (in %). The number of samples analysed is indicated above each boxplot. The bottom and top lines correspond to the 25th and 75th percentiles, respectively. The full line represents the median values. The ends of the whiskers are the 10th and 90th percentiles.

monochromatic light (313 nm) and hydroxyl radical quantum yield (between $\sim 5 \times 10^{-4}$ and 10^{-2}) of six continental cloud water samples. Anastasio and McGregor (2001) investigated the photoreactivity of two cloud waters from the Tenerife Islands to compare the obtained values with fog waters. The authors found $R_{\text{HO}\cdot}^{\text{f}}$, ranging between 3.0 and $6.9 \times 10^{-10} \text{ M s}^{-1}$, which are approximately 1 order of magnitude higher than those reported in this study for marine cloud waters, and the differences can be attributed to the air mass origin, as suggested by Faust and Allen (1993). The authors suggested that long-range terrestrial aerosol and gas transport in continental clouds could provide an additional source of hydroxyl radicals compared with other marine or remote clouds.

3.3 Modelling the hydroxyl radical formation rates

We simulate the hydroxyl formation rate, $R_{\text{HO}\cdot}^{\text{f, mod}}$, using the model along with the relative contribution (%) of each chemical source (Table S3). In Fig. 4, the differences between the modelled and experimental $\text{HO}\cdot$ formation rates are estimated calculating the bias error ($(R_{\text{HO}\cdot}^{\text{f, mod}} - R_{\text{HO}\cdot}^{\text{f, exp}}) / R_{\text{HO}\cdot}^{\text{f, exp}}$ in %). Globally, for the whole cloud water samples (black boxplot), the model can reproduce the range of measured hydroxyl radical formation rates with a slight model underestimation (median of the bias error equal to -23%). However, if the cloud samples are discretized as a function of different iron concentration ranges (boxplots in

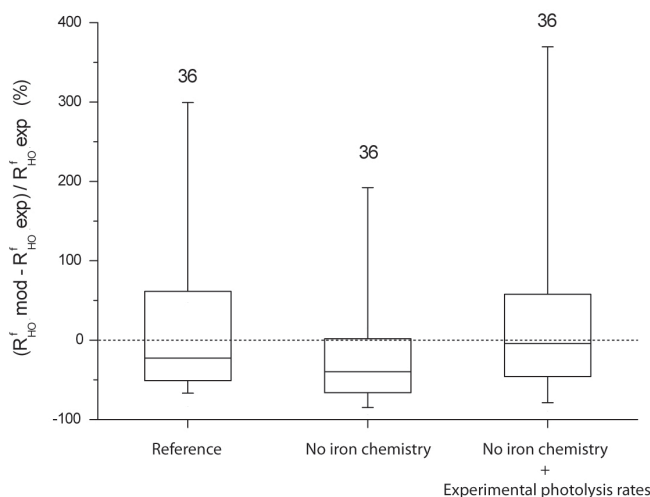


Figure 5. Distribution of the bias error for all cloud water samples for the reference case and for two sensitivity tests performed with the model: (i) with the iron chemistry (photolysis of Fe(III) and the Fenton reaction) neglected in the model; and (ii) with the iron chemistry neglected and the new photolysis rate constants obtained from experimental measurements implemented in the model. The bias error is defined by the ratio $(R_{\text{HO}\cdot}^{\text{f, mod}} - R_{\text{HO}\cdot}^{\text{f, exp}}) / R_{\text{HO}\cdot}^{\text{f, exp}}$ (in %). The number of samples analysed is indicated above each boxplot. The bottom and top lines correspond to the 25th and 75th percentiles, respectively. The full line represents the median values. The ends of the whiskers are the 10th and 90th percentiles.

colour), then the model tends to overestimate the hydroxyl radical formation for iron concentrations ($\text{Fe(II)} + \text{Fe(III)}$) higher than $0.1 \mu\text{M}$. For concentrations of iron between 0.1 and $0.4 \mu\text{M}$ (eight cloud samples), the median of the bias error is 61% whereas for iron concentrations over $0.4 \mu\text{M}$ (five cloud samples) the median reaches 260% . For cloud samples in which the iron concentration is $0.4 \mu\text{M}$, the modelled contribution to the hydroxyl radical formation of iron (Fenton reaction and photolysis of aqua-complexes) can reach 80% (Table S3). In the model, Fe(III) is partially complexed with oxalic acid but the majority of iron for these cloud samples is simulated as aqua-complexes (mainly Fe(OH)_2^{2+} and Fe(OH)_2^+). Therefore, iron can act as a significant $\text{HO}\cdot$ source due to its efficient photolysis (Reactions R7, R8, R9 in Table S1) and the Fenton reaction with H_2O_2 (Reaction R11 in Table S1).

However, in atmospheric natural water, the chemical composition of organic matter is still not very well characterized (Herckes et al., 2013). Part of this organic matter is expected to efficiently complex metals in cloud water (Okochi and Brimblecombe, 2002). Due to missing information about the iron speciation and complexation in natural cloud water, the model probably overestimates the free Fe(III). Moreover, iron organic complexes are not expected to directly generate hydroxyl radicals but primarily contribute to the oxidative capacity via Fe(II) generation and the Fenton process.

Table 3. $R_{\text{HO}\cdot}^f$ (M s^{-1}) and polychromatic quantum yield ($\Phi_{\text{HO}\cdot}$) found in the literature and in this work.

	$R_{\text{HO}\cdot}^f$ (M s^{-1})	Φ_{OH}	References
Rain water	$2.0\text{--}6.5 \times 10^{-11}$		Albinet et al. (2010)
Cloud water	$1.3\text{--}8.3 \times 10^{-10}$	$4.6 \times 10^{-4}\text{--}1.0 \times 10^{-2}$	at 313 nm Faust and Allen (1993)
Fog	$0.9\text{--}6.9 \times 10^{-10}$		
Aqueous extracted aerosol particles	$0.4\text{--}3.8 \times 10^{-10}$	$3.0 \times 10^{-4}\text{--}1.7 \times 10^{-3}$	Arakaki et al. (2006)
Cloud water	$3.1\text{--}6.9 \times 10^{-10}$		Anastasio and McGregor (2001)
Cloud water	$0.3\text{--}5.9 \times 10^{-10}$	$5.1 \times 10^{-4}\text{--}3.0 \times 10^{-3}$	Arakaki and Faust (1998)
Cloud water at the PUY station	$0.2\text{--}4.2 \times 10^{-10}$	$1.3 \times 10^{-5}\text{--}1.0 \times 10^{-2}$	polychromatic This work

Table 4. Modelled photolysis rates calculated by the model versus experimental photolysis rates obtained from experiments reported in Fig. 3.

	Modelled photolysis rates J (s^{-1})	Experimental photolysis rates J (s^{-1})
$\text{H}_2\text{O}_2 \xrightarrow{h\nu} 2 \text{HO}\cdot$	1.52×10^{-6}	$(2.50 \pm 0.11) \times 10^{-6}$
$\text{HNO}_2 \xrightarrow{h\nu} \text{HO}\cdot + \text{NO}\cdot$	6.16×10^{-5}	
$\text{NO}_2^- + \text{H}_2\text{O} \xrightarrow{h\nu} \text{HO}\cdot + \text{NO}\cdot + \text{HO}^-$	9.98×10^{-6}	$(5.15 \pm 0.30) \times 10^{-6}$
$\text{NO}_3^- + \text{H}_2\text{O} \xrightarrow{h\nu} \text{HO}\cdot + \text{NO}_2\cdot + \text{HO}^-$	6.71×10^{-8}	$(1.23 \pm 0.04) \times 10^{-7}$
$\text{Fe}^{3+} + \text{H}_2\text{O} \xrightarrow{h\nu} \text{HO}\cdot + \text{Fe}^{2+} + \text{H}^+$	1.24×10^{-6}	
$\text{Fe}(\text{OH})^{2+} \xrightarrow{h\nu} \text{HO}\cdot + \text{Fe}^{2+}$	2.81×10^{-4}	
$\text{Fe}(\text{OH})_2^+ \xrightarrow{h\nu} \text{HO}\cdot + \text{Fe}^{2+} + \text{HO}^-$	3.53×10^{-4}	

To evaluate this hypothesis, we decide to consider the iron as totally complexed by the organic matter present in natural cloud waters. As a first general approximation, we consider iron as not reactive in the model. The new simulations show that the majority of the simulated values (75 %) of the hydroxyl radical formation rates are now underestimated by the model (median of the bias error equal to -40%) (Fig. 5).

Based on the laboratory irradiation experiments (Sect. 2.6, Fig. 3), new photolysis rates from nitrite, nitrate and hydrogen peroxide are previously estimated from the hydroxyl radical formation rates (Table 4). For nitrate and H_2O_2 , the values calculated by the model are lower than the experimental ones; the experimental photolysis rates are higher by a factor ~ 1.5 for H_2O_2 and ~ 2 for nitrate. For nitrite, the experimental photolysis rate is approximately half of the modelled value. These discrepancies should partially explain the underestimation of $\text{HO}\cdot$ formation by the model. Therefore, we consider the experimental photolysis rates in the model, and a new comparison of modelled $\text{HO}\cdot$ formation rates with experimental values is shown in Fig. 5. The median of the bias error is -3% with the 25th and 75th percentiles at -50 and 60% , respectively. Table S4 reports the distribution of the relative contributions of H_2O_2 , NO_3^- and NO_2^- photolysis to the modelled $R_{\text{HO}\cdot}^f$. While the median values of the ni-

trite and nitrate contributions are calculated by the model as equal to 1 and 5 %, respectively (Fig. 6), the main $\text{HO}\cdot$ contributor is H_2O_2 photolysis (median value of 93 %, with the 25th and 75th percentiles at 85 and 96 %, respectively). This result suggests that H_2O_2 is the key compound that drives the oxidative capacity of our cloud water samples when iron concentrations are relatively low or when iron is suggested to be totally complexed by organic matter.

4 Conclusions

In this study, we compare experimental and modelled $\text{HO}\cdot$ formation rates for 41 cloud water samples with contrasting chemical compositions depending on the origin of the air masses. This approach helps to elucidate the complex aqueous photoreactivity of natural cloud water that is expected to drive the oxidative capacity. Experimental data are obtained considering only the $\text{HO}\cdot$ formation sources with addition of an excess of the chemical probe leading to the measurements of total generated $\text{HO}\cdot$. The first comparison with the M2C2 model shows that the model can reproduce the order of magnitude of measured $R_{\text{HO}\cdot}^f$ (from 1.1×10^{-11} to $4.2 \times 10^{-10} \text{M s}^{-1}$ and from 1.1×10^{-11} to

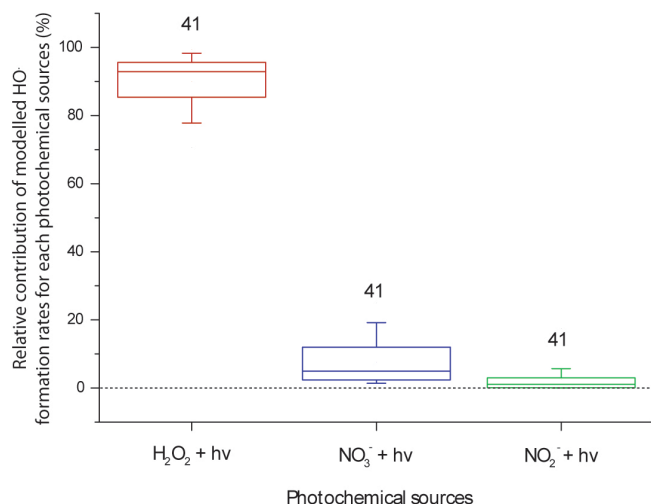


Figure 6. Distribution of relative contributions of modelled HO• formation rates for each photochemical source (H₂O₂, NO₃⁻ and NO₂⁻ photolysis) for all cloud water samples. Model outputs are obtained from the sensitivity test in which the iron chemistry is not considered, and new photolysis rate constants from experimental measurements are implemented in the model. The number of samples analysed is indicated above each boxplot. The bottom and top lines correspond to the 25th and 75th percentiles, respectively. The full line represents the median values. The ends of the whiskers are the 10th and 90th percentiles.

$2.4 \times 10^{-10} \text{ M s}^{-1}$ for experimental and modelled values, respectively). Some discrepancies appear for samples containing iron concentrations over $0.4 \mu\text{M}$ in which the model overestimates the contribution of Fe(III)-aqua complexes to the HO• production rate. Ultimately, the aqueous chemical mechanism in the model was modified considering new photolysis rates for H₂O₂, nitrite and nitrate estimated by laboratory irradiation experiments. As a sensitivity test, iron reactivity was also suppressed in the model to account for the total complexation of iron. The modelled production rates of HO• with the updated mechanism are closer to the experimental values. This supports the hypothesis that iron could be strongly complexed by the organic matter in natural cloud water. These complexes could be more stable and less photoreactive, leading to less HO• production than that calculated by theoretical models in which only the photochemistry of Fe(III) carboxylate is considered (Weller et al., 2014). In this context, evaluation of the complexation of iron by organic compounds in the cloud aqueous phase and the photoreactivity of these complexes should be pursued in future. Their photoreactivity provides significant data to understand the specific role of iron species and, more generally, the oxidant capacity of this medium.

The Supplement related to this article is available online at doi:10.5194/acp-15-9191-2015-supplement.

Acknowledgements. The authors acknowledge the financial support from the Regional Council of Auvergne, from the Observatoire de Physique du Globe de Clermont-Ferrand (OPGC), from the Fédération de Recherche en Environnement through the CPER Environnement founded by Région Auvergne, the French ministry, and FEDER from the European community. This work on the analysis of the cloud water chemical composition is supported by the French Ministry and CNRS-INSU. The authors are very grateful to the Agence Nationale de la Recherche (ANR) for its financial support through the BIOCAP project (ANR-13-BS06-0004) and the CUMULUS project (ANR-10-BLAN-0617).

Edited by: N. L. Ng

References

- Albinet, A., Minero, C., and Vione, D.: Photochemical generation of reactive species upon irradiation of rainwater: Negligible photoactivity of dissolved organic matter, *Sci. Total Environ.*, 408, 3367–3373, 2010.
- Altieri, K. E., Seitzinger, S. P., Carlton, A. G., Turpin, B. J., Klein, G. C., and Marshall, A. G.: Oligomers formed through in-cloud methylglyoxal reactions: chemical composition, properties, and mechanisms investigated by ultra-high resolution FT-ICR mass spectrometry, *Atmos. Environ.*, 42, 1476–1490, 2008.
- Anastasio, C. and McGregor, K. G.: Chemistry of fog waters in California's Central Valley: 1. In situ photoformation of hydroxyl radical and singlet molecular oxygen, *Atmos. Environ.*, 35, 1079–1089, 2001.
- Arakaki, T. and Faust, B. C.: Sources, sinks, and mechanisms of hydroxyl radical (OH) photoproduction and consumption in authentic acidic continental cloud waters from Whiteface Mountain, New York: The role of the Fe(r) (r = II, III) photochemical cycle, *J. Geophys. Res.*, 103, 3487–3504, doi:10.1029/97jd02795, 1998.
- Arakaki, T., Kuroki, Y., Okada, K., Nakama, Y., Ikota, H., Kinjo, M., Higuchi, T., Uehara, M., and Tanahara, A.: Chemical composition and photochemical formation of hydroxyl radicals in aqueous extracts of aerosol particles collected in Okinawa, Japan, *Atmos. Environ.*, 40, 4764–4774, 2006.
- Arakaki, T., Anastasio, C., Kuroki, Y., Nakajima, H., Okada, K., Kotani, Y., Handa, D., Azechi, S., Kimura, T., Tshuhako, A., and Miyagi, Y.: A general scavenging rate constant for reaction of hydroxyl radical with organic carbon in atmospheric waters, *Environ. Sci. Technol.*, 47, 8196–8203, doi:10.1021/es401927b, 2013.
- Brantner, B., Fierlinger, H., Puxbaum, H., and Berner, A.: Cloud-water chemistry in the subcooled droplet regime at Mount Sonnblick (3106 m a.s.l., Salzburg, Austria), *Water Air Soil Pollut.*, 74, 363–384, 1994.
- Carlton, A. G., Turpin, B. J., Altieri, K. E., Seitzinger, S., Reff, A., Lim, H.-J., and Ervens, B.: Atmospheric oxalic acid and SOA production from glyoxal: results of aqueous photooxidation experiments, *Atmos. Environ.*, 41, 7588–7602, 2007.
- Charbouillot, T., Brigante, M., Mailhot, G., Maddigapu, P. R., Minero, C., and Vione, D.: Performance and selectivity of the terephthalic acid probe for OH as a function of temperature, pH and composition of atmospherically relevant

- aqueous media, *J. Photochem. Photobiol. A*, 222, 70–76, doi:10.1016/j.jphotochem.2011.05.003, 2011.
- Charbouillot, T., Gorini, S., Vyard, G., Parazols, M., Brigante, M., Deguillaume, L., Delort, A.-M., and Mailhot, G.: Mechanism of carboxylic acid photooxidation in atmospheric aqueous phase: Formation, fate and reactivity, *Atmos. Environ.*, 56, 1–8, doi:10.1016/j.atmosenv.2012.03.079, 2012.
- Deguillaume, L., Leriche, M., Monod, A., and Chaumerliac, N.: The role of transition metal ions on HO_x radicals in clouds: a numerical evaluation of its impact on multiphase chemistry, *Atmos. Chem. Phys.*, 4, 95–110, doi:10.5194/acp-4-95-2004, 2004.
- Deguillaume, L., Leriche, M., Desboeufs, K., Mailhot, G., George, C., and Chaumerliac, N.: Transition metals in atmospheric liquid phases: sources, reactivity, and sensitive parameters, *Chem. Rev.*, 105, 3388–3431, doi:10.1021/cr040649c, 2005.
- Deguillaume, L., Charbouillot, T., Joly, M., Väitilingom, M., Parazols, M., Marinoni, A., Amato, P., Delort, A.-M., Vinatier, V., Flossmann, A., Chaumerliac, N., Pichon, J. M., Houdier, S., Laj, P., Sellegri, K., Colomb, A., Brigante, M., and Mailhot, G.: Classification of clouds sampled at the puy de Dôme (France) based on 10 yr of monitoring of their physicochemical properties, *Atmos. Chem. Phys.*, 14, 1485–1506, doi:10.5194/acp-14-1485-2014, 2014.
- De Haan, D. O., Tolbert, M. A., and Jimenez, J. L.: Atmospheric condensed-phase reactions of glyoxal with methylamine, *Geophys. Res. Lett.*, 36, L11819, doi:10.1029/2009gl037441, 2009.
- Deming, S. N., Michotte, Y., Massart, D. L., Kaufman, L., and Vandeginste, B. G. M.: *Chemometrics: A textbook*, 1st Edn., Elsevier Science, doi:10.1016/0169-7439(89)80019-X, 1988.
- Dulin, D. and Mill, T.: Development and evaluation of sunlight actinometers, *Environ. Sci. Technol.*, 16, 815–820, doi:10.1021/es00105a017, 1982.
- Ervens, B. and Volkamer, R.: Glyoxal processing by aerosol multiphase chemistry: towards a kinetic modeling framework of secondary organic aerosol formation in aqueous particles, *Atmos. Chem. Phys.*, 10, 8219–8244, doi:10.5194/acp-10-8219-2010, 2010.
- Ervens, B., Turpin, B. J., and Weber, R. J.: Secondary organic aerosol formation in cloud droplets and aqueous particles (aqSOA): a review of laboratory, field and model studies, *Atmos. Chem. Phys.*, 11, 11069–11102, doi:10.5194/acp-11-11069-2011, 2011.
- Ervens, B., Sorooshian, A., Lim, Y. B., and Turpin, B. J.: Key parameters controlling OH-initiated formation of secondary organic aerosol in the aqueous phase (aqSOA), *J. Geophys. Res.-Atmos.*, 119, 3997–4016, doi:10.1002/2013jd021021, 2014.
- Faust, B. C. and Allen, J. M.: Aqueous-phase photochemical formation of hydroxyl radical in authentic cloudwaters and fogwaters, *Environ. Sci. Technol.*, 27, 1221–1224, doi:10.1021/es00043a024, 1993.
- Herckes, P., Valsaraj, K. T., and Collett Jr., J. L.: A review of observations of organic matter in fogs and clouds: Origin, processing and fate, *Atmos. Res.*, 132–133, 434–449, doi:10.1016/j.atmosres.2013.06.005, 2013.
- Herrmann, H., Hoffmann, D., Schaefer, T., Brüner, P., and Tilgner, A.: Tropospheric aqueous-phase free-radical chemistry: radical sources, spectra, reaction kinetics and prediction tools, *Chem. Phys. Chem.*, 11, 3796–3822, doi:10.1002/cphc.201000533, 2010.
- Hervo, M.: Etude des propriétés optiques et radiatives des aérosols en atmosphère réelle: Impact de l'hygroscopicité, PhD thesis, Blaise Pascal University, Aubiere, 2013.
- HYSPLIT (HYbrid Single-particle Lagrangian Integrated Trajectory) Model Access via NOAA ARL READY Website, available at: <http://ready.arl.noaa.gov/HYSPLIT.php> (last access: 23 February 2015), 2012.
- Kieber, R. J. and Seaton, P. J.: Determination of subnanomolar concentrations of nitrite in natural waters, *Anal. Chem.*, 67, 3261–3264, doi:10.1021/ac00114a024, 1995.
- Lê, S., Josse, J., and Husson, F.: FactoMineR: An R Package for Multivariate Analysis, *J. Stat. Softw.*, 25, 1–18, 2008.
- Leriche, M., Voisin, D., Chaumerliac, N., Monod, A., and Aumont, B.: A model for tropospheric multiphase chemistry: application to one cloudy event during the CIME experiment, *Atmos. Environ.*, 34, 5015–5036, doi:10.1016/S1352-2310(00)00329-0, 2000.
- Leriche, M., Chaumerliac, N., and Monod, A.: Coupling quasi-spectral microphysics with multiphase chemistry: a case study of a polluted air mass at the top of the Puy de Dôme mountain (France), *Atmos. Environ.*, 35, 5411–5423, doi:10.1016/S1352-2310(01)00300-4, 2001.
- Long, Y., Charbouillot, T., Brigante, M., Mailhot, G., Delort, A.-M., Chaumerliac, N., and Deguillaume, L.: Evaluation of modeled cloud chemistry mechanism against laboratory irradiation experiments: The HxOy/iron/carboxylic acid chemical system, *Atmos. Environ.*, 77, 686–695, doi:10.1016/j.atmosenv.2013.05.037, 2013.
- Madronich, S. and Flocke, S.: The Role of Solar Radiation in Atmospheric Chemistry, in: *Environmental Photochemistry*, edited by: Boule, P., *The Handbook of Environmental Chemistry*, Springer Berlin Heidelberg, 1–26, 1999.
- Miller, W. L. and Kester, D. R.: Hydrogen peroxide measurement in seawater by (p-hydroxyphenyl)acetic acid dimerization, *Anal. Chem.*, 60, 2711–2715, doi:10.1021/ac00175a014, 2002.
- Neta, P., Huie, R. E., and Ross, A. B.: Rate constants for reactions of inorganic radicals in aqueous solution, *J. Phys. Chem. Ref. Data*, 17, 1027–1284, doi:10.1063/1.555808, 1988.
- Okochi, H. and Brimblecombe, P.: Potential trace metal-organic complexation in the atmosphere, *Sci. World J.*, 2, 767–786, doi:10.1100/tsw.2002.132, 2002.
- Parazols, M., Marinoni, A., Amato, P., Abida, O., Laj, P., and Mailhot, G.: Speciation and role of iron in cloud droplets at the puy de Dome station, *J. Atmos. Chem.*, 54, 267–281, doi:10.1007/s10874-006-9026-x, 2006.
- Perri, M. J., Seitzinger, S., and Turpin, B. J.: Secondary organic aerosol production from aqueous photooxidation of glycolaldehyde: Laboratory experiments, *Atmos. Environ.*, 43, 1487–1497, doi:10.1016/j.atmosenv.2008.11.037, 2009.
- R Core Team: a language and environment for statistical computing R, foundation for Statistical Computing, available at: <http://www.R-project.org/> (last access: 17 January 2015), 2013.
- Seinfeld, J. H. and Pandis, S. N.: *Atmospheric Chemistry and Physics: From Air Pollution to Climate Change*, 2nd Edn., 2006.
- Stookey, L. L.: Ferrozine – a new spectrophotometric reagent for iron, *Anal. Chem.*, 42, 779–781, doi:10.1021/ac60289a016, 1970.
- Tan, Y., Lim, Y. B., Altieri, K. E., Seitzinger, S. P., and Turpin, B. J.: Mechanisms leading to oligomers and SOA through aqueous

- ous photooxidation: insights from OH radical oxidation of acetic acid and methylglyoxal, *Atmos. Chem. Phys.*, 12, 801–813, doi:10.5194/acp-12-801-2012, 2012.
- Tilgner, A. and Herrmann, H.: Radical-driven carbonyl-to-acid conversion and acid degradation in tropospheric aqueous systems studied by CAPRAM, *Atmos. Environ.*, 44, 5415–5422, doi:10.1016/j.atmosenv.2010.07.050, 2010.
- Vaitilingom, M., Deguillaume, L., Vinatier, V., Sancelme, M., Amato, P., Chaumerliac, N., and Delort, A.-M.: Potential impact of microbial activity on the oxidant capacity and organic carbon budget in clouds, *Proc. Natl. Acad. Sci.*, 110, 559–564, doi:10.1073/pnas.1205743110, 2013.
- Weller, C., Tilgner, A., Brauer, P., and Herrmann, H.: Modeling the impact of iron-carboxylate photochemistry on radical budget and carboxylate degradation in cloud droplets and particles, *Environ. Sci. Technol.*, 48, 5652–5659, doi:10.1021/es4056643, 2014.
- Yu, X.-Y. and Barker, J. R.: Hydrogen peroxide photolysis in acidic aqueous solutions containing chloride ions. II. Quantum yield of HO(aq) radicals, *J. Phys. Chem. A*, 107, 1325–1332, doi:10.1021/jp026666s, 2003.
- Zafiriou, O. C. and Bonneau, R.: Wavelength-dependent quantum yield of OH radical formation from photolysis of nitrite ions in water, *Photochem. Photobiol.*, 45, 723–727, doi:10.1111/j.1751-1097.1987.tb07873.x, 1987.
- Zellner, R., Exner, M., and Herrmann, H.: Absolute OH quantum yields in the laser photolysis of nitrate, nitrite and dissolved H₂O₂ at 308 and 351 nm in the temperature range 278–353 K, *J. Atmos. Chem.*, 10, 411–425, doi:10.1007/bf00115783, 1990.